

Detection and extraction of signals from the epoch of reionization using higher order one-point statistics

Geraint J. A. Harker,^{1*} Saleem Zaroubi,¹ Rajat M. Thomas,¹ Vibor Jelić,¹ Panagiotis Labropoulos,¹ Garrelt Mellema,² Ilian T. Iliev,³ Gianni Bernardi,¹ Michiel A. Brentjens,⁴ A. G. de Bruyn,^{1,4} Benedetta Ciardi,⁵ Leon V. E. Koopmans,¹ V. N. Pandey,¹ Andreas H. Pawlik,⁶ Joop Schaye⁶ and Sarod Yatawatta¹

¹*Kapteyn Astronomical Institute, University of Groningen, PO Box 800, 9700AV Groningen, the Netherlands*

²*Department of Astronomy, Alba Nova University Centre, Stockholm University, SE-106 91 Stockholm, Sweden*

³*Institute for Theoretical Physics, Winterthurerstrasse 190, CH-8057 Zürich, Switzerland*

⁴*ASTRON, Postbus 2, 7990AA Dwingeloo, the Netherlands*

⁵*Max-Planck Institute for Astrophysics, Karl-Schwarzschild-Straße 1, 85748 Garching, Germany*

⁶*Leiden Observatory, Leiden University, PO Box 9513, 2300RA Leiden, the Netherlands*

31 October 2018

ABSTRACT

Detecting redshifted 21cm emission from neutral hydrogen in the early Universe promises to give direct constraints on the epoch of reionization (EoR). It will, though, be very challenging to extract the cosmological signal (CS) from foregrounds and noise which are orders of magnitude larger. Fortunately, the signal has some characteristics which differentiate it from the foregrounds and noise, and we suggest that using the correct statistics may tease out signatures of reionization. We generate mock datacubes simulating the output of the Low Frequency Array (LOFAR) EoR experiment. These cubes combine realistic models for Galactic and extragalactic foregrounds and the noise with three different simulations of the CS. We fit out the foregrounds, which are smooth in the frequency direction, to produce residual images in each frequency band. We denoise these images and study the skewness of the one-point distribution in the images as a function of frequency. We find that, under sufficiently optimistic assumptions, we can recover the main features of the redshift evolution of the skewness in the 21cm signal. We argue that some of these features – such as a dip at the onset of reionization, followed by a rise towards its later stages – may be generic, and give us a promising route to a statistical detection of reionization.

Key words: cosmology: theory – diffuse radiation – methods: statistical – radio lines: general

1 INTRODUCTION

Between redshift $z \approx 20$ and $z \approx 6$ the Universe underwent a transition from being almost entirely neutral to almost entirely ionized (Benson et al. 2006; Furlanetto, Oh & Briggs 2006). This period, the epoch of reionization (EoR), saw the first collapsed objects emit radiation which heated and ionized the surrounding diffuse gas (additional sources of heating and ionization, such as dark matter decay, have also been considered; see, e.g., Valdés et al. 2007). Studying the emission from this gas, in particular the redshifted 21cm line of neutral hydrogen (Field 1958, 1959; Hogan & Rees 1979; Scott & Rees 1990; Kumar, Subramanian & Padmanabhan 1995; Madau, Meiksin & Rees 1997), may therefore tell us about the physics of these objects, and about structure formation in a redshift range that has previously been explored rather less directly.

For example, quasar absorption spectra can constrain the properties of the intergalactic medium towards the end of reionization (Fan et al. 2006), while measurements of temperature and polarization anisotropies in the cosmic microwave background provide an integral constraint on the density of free electrons between the observer and the surface of last scattering (e.g. Dunkley et al. 2008).

Several current and upcoming facilities (e.g. GMRT,¹ MWA,² LOFAR,³ 21CMA,⁴ PAPER,⁵ SKA⁶) will be sensitive to emission of the right wavelength to detect a signal from neutral hydrogen during the EoR. Significant observational challenges must be

¹ Giant Metrewave Radio Telescope, <http://www.gmrt.ncra.tifr.res.in/>

² Murchison Widefield Array, <http://www.haystack.mit.edu/ast/arrays/mwa/>

³ Low Frequency Array, <http://www.lofar.org/>

⁴ 21 Centimeter Array, <http://web.phys.cmu.edu/~past/>

⁵ Precision Array to Probe EoR, <http://astro.berkeley.edu/~dbacker/eor/>

⁶ Square Kilometre Array, <http://www.skatelescope.org/>

* E-mail: harker@astro.rug.nl

overcome, however, before a convincing detection can be made. The Galactic and extragalactic foregrounds have a mean amplitude around 4–5 orders of magnitude larger than the expected EoR signal (though their fluctuations, which are the relevant quantity for an interferometer, are only around three orders of magnitude larger; see, e.g., Shaver et al. 1999). Even closer to home, the signal is corrupted by the ionosphere, radio frequency interference and instrumental effects. Assuming all these factors can be dealt with, for realistic integration times with the imminent generation of facilities the random noise on the measurement per resolution element will still be a few times larger than the signal.

The prospect of new observations of a poorly constrained period in the Universe’s history also poses a challenge to theorists: to model and characterize the 21cm emission in such a way that it can be meaningfully compared to the data (e.g. Barkana & Loeb 2001; Loeb & Barkana 2001; Ciardi, Ferrara & White 2003; Ciardi, Stoehr & White 2003; Bromm & Larson 2004; Gleser et al. 2006; Iliev et al. 2006, 2008; Zaroubi et al. 2007; Thomas & Zaroubi 2008). Given the observational limitations listed above, it is unlikely that there will soon be clean maps of the EoR signal with which to confront models. The first detection of reionization from redshifted 21cm data will therefore be of a statistical nature. This raises the question of precisely which statistics to use: a question discussed by, e.g., Furlanetto, Zaldarriaga & Hernquist (2004a,b); Bharadwaj & Ali (2005); Gleser, Nusser & Benson (2008). In the first instance, they should provide a clear indication of the global transition from a Universe that is mostly neutral to one that is mostly ionized. Ideally, they should be able to discriminate between different models describing the more detailed progress of reionization. Most importantly, though, they should be robust to the contamination introduced by the observing process, and to the presence of high levels of noise.

We propose using the skewness of the one-point distribution of the brightness temperature to study reionization, though we also consider the prospects of other, similar statistics: the unnormalized third moment and the kurtosis of the distribution. As we shall see below, general arguments suggest that the skewness should be a strongly evolving function of redshift during the EoR, and these arguments are supported by simulations. Using these simulations, we generate datacubes which also incorporate realistic models for the foregrounds, instrumental response and noise levels expected for the LOFAR EoR experiment. We generate residual images at each observed frequency by attempting to remove the foregrounds using a fitting algorithm, then study the properties of these residual images as a function of redshift. If these residual images are de-noised appropriately, we find that we can indeed track the progress of reionization using the skewness.

In Section 2 we introduce the skewness and explain how it may help. In Section 3 we give a brief description of our models for the cosmological signal (CS), instrumental response, foregrounds and noise. Then, in Section 4, we describe our method for extracting the signal from datacubes which combine all these components, and present our results. We discuss some possible problems with and extensions to our methods in Section 5, and finally we offer some conclusions in Section 6.

2 GENERAL APPROACH

We assume, with reasonable observational support, that the foregrounds are smooth as a function of frequency, and exploit this in

order to extract the CS (Shaver et al. 1999; Di Matteo et al. 2002; Oh & Mack 2003; Zaldarriaga, Furlanetto & Hernquist 2004). A simple way to imagine doing this is first to estimate the foregrounds, either by fitting a smooth function to the intensity as a function of frequency along each line of sight, or by applying a filtering procedure. Subtracting this estimate from the total yields fitting residuals which are an estimate of the CS plus random noise.

If the variance of the noise is known, then at each frequency (or equivalently at each redshift) we can attribute excess variance in the fitting residuals over and above this level as coming from the CS. This may yield a statistical detection of emission from the epoch of reionization. Jelić et al. (2008) demonstrate this method using the same foregrounds and noise levels as are used in this work.

There are some difficulties with both parts of the above procedure. Firstly, we may over-fit or under-fit, leading (respectively) to underestimating or overestimating the residuals. This problem is exacerbated near the ends of the frequency range. Secondly, the noise properties may not be sufficiently well characterized. The variance of the signal is expected to be only a small fraction of the variance of the noise, and hence the latter must be very well known.

We therefore seek a statistic on the fitting residuals which will detect the onset of reionization more robustly with respect to errors in our estimates of the variance. A possible candidate is the skewness, γ_1 , defined in general for a continuous distribution with probability density function $f(x)$ as

$$\gamma_1 \equiv \frac{\mu_3}{\sigma^3} \equiv \frac{\int_{-\infty}^{\infty} (x - \mu)^3 f(x) dx}{\left(\int_{-\infty}^{\infty} (x - \mu)^2 f(x) dx \right)^{\frac{3}{2}}} \quad (1)$$

where σ^2 is the variance of the distribution and μ_3 is the third moment about its mean, μ . A distribution which is mainly concentrated at low x , but with a tail towards high x , will have positive skewness. Similarly, a distribution with a tail extending to low x will have negative skewness, and a poor estimate of σ cannot change its sign.

Rather than dealing with a continuous distribution, we will be computing the skewness for images with N pixels, in which the i th pixel has a temperature T_i . Then the skewness may be expressed as

$$\gamma_1 = \frac{\frac{1}{N} \sum_i (T_i - \bar{T})^3}{\left(\frac{1}{N} \sum_i (T_i - \bar{T})^2 \right)^{\frac{3}{2}}} \quad (2)$$

where \bar{T} is the mean temperature in that image and the sums are over all pixels. In the case of residual images, if the foreground fitting is unbiased, and if the noise is not skewed, then any significant skewness remaining must come from the cosmological signal. Moreover, we may expect some skewness in the cosmological signal, which becomes very non-Gaussian once ionized bubbles appear in large numbers during reionization.

To be concrete, making some reasonable assumptions and approximations (that the optical depth is much less than unity, that the spin temperature of the neutral hydrogen is much greater than the CMB temperature, and that at these redshifts the Hubble parameter $H(z) \approx \Omega_m^{1/2} H_0 (1+z)^{3/2}$), the difference, δT_b , between the brightness temperature of the 21cm emission and the CMB is given by (Madau et al. 1997; Ciardi & Madau 2003)

$$\frac{\delta T_b}{mK} = 39h(1+\delta)x_{\text{HI}} \left(\frac{\Omega_b}{0.042} \right) \left[\left(\frac{0.24}{\Omega_m} \right) \left(\frac{1+z}{10} \right) \right]^{\frac{1}{2}} \quad (3)$$

where δ is the matter density contrast, x_{HI} is the neutral hy-

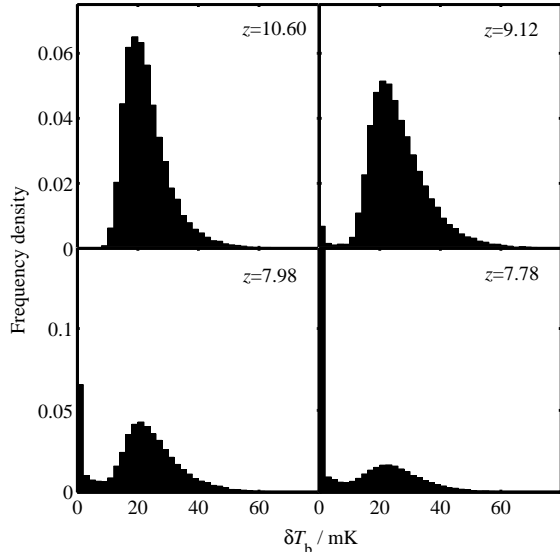


Figure 1. The distribution of δT_b in the f250C simulation (see Section 3.1) at four different redshifts, showing how the distribution evolves as reionization proceeds. Note that the y-axis scale in the top two panels is different from that in the bottom two panels. The delta-function at $\delta T_b = 0$ grows throughout this period while the rest of the distribution retains a similar shape. The bar for the first bin in the bottom-right panel has been cut off: approximately 58 per cent of points are in the first bin at $z = 7.78$.

drogen fraction, and the current value of the Hubble parameter, $H_0 = 100h \text{ km s}^{-1} \text{ Mpc}^{-1}$.

At high redshift, when x_{HI} is close to unity everywhere, the distribution of intensities is governed by the density field, $1 + \delta$. Initially this is nearly Gaussian, but develops a positive skewness due to gravitational instabilities: see, for example, Peebles (1980). This period is illustrated in the top left panel of Fig. 1, which shows the one-point distribution of δT_b in one of our simulations (the f250C simulation; see Section 3.1) at $z = 10.6$, corresponding to an observed frequency of 122.5 MHz. If reionization then takes place in patches, with large volumes remaining mostly neutral while almost fully ionized bubbles form around sources of ionizing photons, this has the effect of setting $x_{\text{HI}} = 0$ (and so $\delta T_b = 0$) within the bubbles, affecting the distribution of δT_b outside the bubbles only weakly. So, in an idealized case, reionization takes points from the distribution of δT_b and moves them to a Dirac delta-function at zero. This has the effect of making the skewness less positive; it may even become negative. The distribution of δT_b at an early stage in this process ($z = 9.12$, or 140.3 MHz) is shown in the top right panel of Fig. 1. By $z = 7.98$ (158.2 MHz; bottom-left panel) the two parts of the distribution are very distinct. This may help to make it clear how the skewness can vanish: the mean δT_b lies between these two peaks, and the negative contribution to the skewness from points in the delta function at zero may cancel with the positive contribution from points to the right. At a later stage of reionization, when most of the pixels in a noiseless map of δT_b at a given frequency have values near zero, the points outside ionized bubbles form a high- δT_b tail, giving the overall distribution a strong positive skew. This can be seen in the bottom right panel of Fig. 1 ($z = 7.78$ or 161.8 MHz). Note the short time between the third and fourth panels: the later stages of reionization can progress rather quickly as the number of ionizing sources can

rise very rapidly, especially if a major part is played by massive sources residing in haloes in the exponential tail of the mass function (Jenkins et al. 2001).

In this idealized case, then, the skewness as a function of redshift should show a dip in the early stages of reionization, before growing large in the later stages. Our aim in the subsequent sections of this paper is to test if such a characteristic feature is indeed seen in realistic simulations of reionization, and whether or not it can provide a robust detection; or in other words, whether the effects of foreground subtraction, noise, and instrumental corruption can mask or mimic the signal.

3 SIMULATIONS

3.1 Cosmological signal

We use three simulations to estimate the CS. The first and most detailed is the simulation labelled f250C by Iliev et al. (2008). The methodology behind this simulation is more fully described by Iliev et al. (2006) and Mellema et al. (2006b). The cosmological particle-mesh code PMFAST (Merz, Pen & Trac 2005) was used to follow the distribution of dark matter, using 1624^3 particles on a 3248^3 mesh. The ionization fraction was then calculated in post-processing using the radiative transfer and non-equilibrium chemistry code C²-RAY (Mellema et al. 2006a). This takes place on a coarser, 203^3 mesh, and this is therefore the size used in this work. The simulation box has a comoving size of $100 h^{-1} \text{ Mpc}$. The cosmological parameters are close to those inferred from the three-year *Wilkinson Microwave Anisotropy Probe* data (WMAP3: Spergel et al. 2007), namely $(\Omega_m, \Omega_\Lambda, \Omega_b, h, \sigma_8, n) = (0.24, 0.76, 0.042, 0.73, 0.74, 0.95)$.

A slightly different approach, detailed by Thomas et al. (2009), is used to generate our other simulations. The dark matter distribution is calculated using the TREE-PM N -body code GADGET2 (Springel, Yoshida & White 2001; Springel 2005). Ionization is then calculated using a one-dimensional radiative transfer code (Thomas & Zaroubi 2008). The speed of this approach means it is possible to study many more alternative scenarios for the reionization process, while retaining good agreement with more accurate, three-dimensional radiative transfer simulations. We will show results from two different simulations. In both cases, the dark matter simulation uses 512^3 dark matter particles in a box of comoving size $100 h^{-1} \text{ Mpc}$, with $(\Omega_m, \Omega_\Lambda, \Omega_b, h, \sigma_8, n) = (0.238, 0.762, 0.0418, 0.73, 0.74, 0.951)$. While the simulations contain no baryons, this value of Ω_b was used to generate the initial power spectrum. These parameters give them lower resolution than the dark matter part of the f250C simulation, meaning that low mass sources are not resolved and are neglected. In one of these simulations we assume that the Universe is reionized by QSOs, and in the other by stars. These two simulations are labelled ‘T-QSO’ and ‘T-star’ respectively. The former should not be affected too seriously by the lack of resolution, since QSOs do not reside in low-mass haloes. In the latter, the geometry of reionization may be altered: compared to a higher resolution simulation, larger ionized bubbles may form at a given global star formation rate, for example. As we shall see below, ‘T-star’ shows rather different characteristics from the f250C simulation, despite the fact that stars provide the ionizing photons in both cases. This illustrates the uncertainties involved in modelling the physics of reionization, in selecting the source populations and finding their distribution in space, and in choosing

the approximations required to make the calculations tractable. We do not analyze the differences between the simulations in great detail here; rather, we use the different simulations to provide a variety of plausible scenarios with which to test our signal extraction techniques.

The above calculations all take place in periodic boxes. The final step in generating a datacube is to take a series of simulation snapshots at different redshifts, and interpolate between them to produce a spatial slice at each observed frequency. This procedure, which is described in detail by Thomas et al. (2009) and Mellema et al. (2006b), is analogous to the generation of lightcone output to compare to galaxy surveys (Evrard et al. 2002). In performing this conversion from a position in a periodic box to a redshift, we take account of the peculiar velocities; that is, our datacubes are in redshift space, as will be the case for the observational data. As emphasized by Mellema et al. (2006b), who were the first to include peculiar velocity distortions in a redshifted 21cm context based on detailed simulations, these effects can be important. At linear scales, the redshift space distortions have the effect of enhancing density fluctuations along the line of sight (Kaiser 1987; Bharadwaj & Ali 2005).

3.2 Foregrounds, noise and instrumental effects

We use the foreground simulations described in detail by Jelić et al. (2008). These incorporate contributions from Galactic diffuse synchrotron and free-free emission, and supernova remnants. They also include extragalactic foregrounds from radio galaxies and radio clusters. The foreground maps cover an area $5^\circ \times 5^\circ$ on the sky, which corresponds to the area of one LOFAR EoR window. We also adopt the frequency-dependent noise levels given by Jelić et al. (2008). The noise is described in more detail below, when we introduce each of our two noise models.

In Section 4, we will give results obtained by combining the CS, foregrounds and noise, and then attempting to extract the CS. We also attempt the more difficult, and more realistic task of extracting the signal given such a datacube corrupted by the instrumental response (so-called ‘dirty maps’). These instrumental effects will be described in more detail by Labropoulos et al. (2009). In brief, at each observed frequency, each pair of LOFAR stations gives an estimate of the Fourier transform of the sky brightness along a track of points (a uv track) in Fourier space (the uv plane). Translated into configuration space, this means that our images of the sky are convolved with a complicated point spread function (the ‘dirty beam’). Moreover, because the origin of the Fourier plane is not sampled, interferometer measurements are not sensitive to the mean brightness. A more detailed introduction to such datacubes, and their relation to the power spectrum of emission from the EoR, is given by Morales & Hewitt (2004).

4 RESULTS

4.1 Skewness in perfect data

The evolution of skewness in our three simulations, uncorrupted by noise or foregrounds, for the redshift range observable by LOFAR, is given in Fig. 2. The most obvious feature here, common to all three simulations, is the rise in the skewness at low redshift, due to the high- δT_b tail of points with some remaining neutral hydrogen. At higher redshift there are some differences, however. In f250C there is a clear dip at $z \sim 7.8$ – 9 , whereas this is not so obvious in

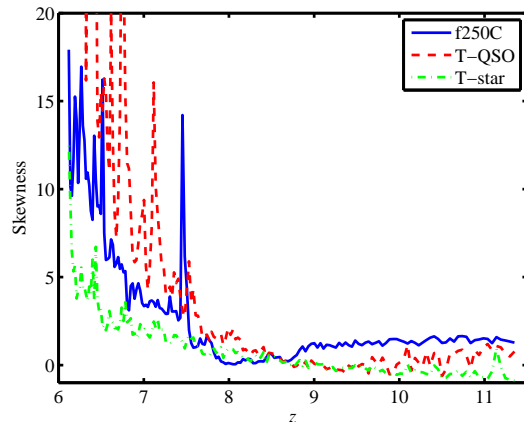


Figure 2. The evolution of the skewness of the distribution of δT_b as a function of redshift in our three simulations. Each point corresponds to the skewness of the one-point distribution in a slice through a datacube at the given redshift. The most striking feature here is the steep rise in skewness at low redshift. The details at high redshift can be seen more clearly in Fig. 3.

either of the other simulations. For the T-QSO simulation, though, and more noticeably for the T-star simulation, the skewness is negative in certain redshift slices. All the simulations show large spikes in skewness at low redshift. At these redshifts, a slice may have only one or a few regions from which there is significant emission. This leads to large variation between slices. A slice in which one small region produces a high-emission tail in the one-point distribution, and which is surrounded by more uniform slices, shows up as a spike in the evolution of the skewness.

The lower-skewness region of the plot is shown in more detail in Fig. 3, where we also compare the evolution of the skewness to that of the mean. Whilst the mean value of δT_b is unobservable with an interferometer such as LOFAR, this serves to illustrate the progress of reionization. Clearly the process is much more rapid in f250C than in the T-QSO simulation, which in turn is more rapid than the T-star simulation. In Fig. 3 a dip in the skewness is discernible in T-QSO, but is much less obvious than the dip in f250C because of fluctuations at high redshift, and because it spans a wider range in redshift due to the more extended reionization. This may be an indication that a more extended reionization process will be harder to detect using the skewness. The T-star simulation provides some hope, however. Despite an even more gradual reduction in the mean differential brightness temperature, the skewness is negative for quite a large range in redshift. Because the density field is positively skewed, a negative skewness is a clear signature of reionization. It is therefore possible that the skewness could provide a detection even in the case of very extended reionization.

4.2 Extracted skewness

We now proceed to test the possibilities for signal extraction using the skewness, starting with a rather more optimistic case than will be encountered with the actual LOFAR EoR experiment. We first note that the $5^\circ \times 5^\circ$ field of one LOFAR EoR window corresponds to a distance of approximately $800 \text{ Mpc} \times 800 \text{ Mpc}$ (comoving) at $z = 10$ in our assumed cosmology. At each redshift we therefore tile copies of the simulation to produce a slice of the correct size, then interpolate this onto a 256^2 mesh. Since each pixel will be affected differently by foregrounds and noise, and since we con-

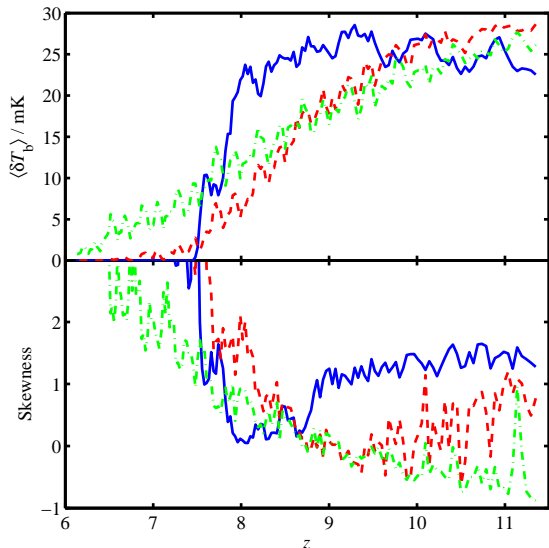


Figure 3. The evolution of the mean differential brightness temperature (top panel) and of the skewness (bottom panel) in the three simulations. The colours and styles of the lines are the same as in Fig. 2. The top panel shows that reionization is extended to very different degrees in the different simulations. We cut off the large values of the skewness in the bottom panel so that the dip in skewness at high redshift can be seen more clearly than in Fig. 2.

consider only one-point statistics, we do not anticipate that this will strongly affect our conclusions. To produce our datacube, we add the simulated foregrounds described in Section 3.2 to the CS, then smooth each slice using a Gaussian kernel to the estimated LO-FAR resolution of ≈ 4 arcmin. We then add uncorrelated random noise as described by Jelić et al. (2008). The noise has an *rms* of 52 mK at 150 MHz and has two contributions: a frequency dependent component coming from the sky, which scales as $\nu^{-2.55}$, and a frequency-independent part from the receivers. The noise on each image pixel is independent. In reality, this will not be the case: rather, the noise on individual visibilities will be independent. We will tackle this more difficult case with realistic noise and a non-Gaussian point spread function below. Spatial slices are separated by 0.5 MHz in frequency, ν . At 150 MHz this corresponds to a difference in redshift, $\Delta z \approx 0.03$, the slices having a comoving thickness of approximately $7 h^{-1}$ Mpc.

Once we have a datacube with EoR signal, foregrounds and noise, we fit a third-order polynomial in $\log \nu$ to each pixel. We have experimented with using different functional forms, but find that so long as we obtain a visually reasonable fit, our results for the skewness do not change enough to affect our conclusions. Measurements of the variance are rather more sensitive to under- and over-fitting, which demonstrates the importance of understanding the foregrounds well, and of using robust statistics. It is also possible to estimate the foregrounds by removing noise using a filtering procedure. While this requires fewer assumptions about the nature of the foregrounds, it tends to over-fit.

After a fit has been obtained, it is subtracted from the total, leaving residuals which are an estimate of the CS plus the noise. The skewness of these residuals as a function of redshift is shown in Fig. 4. While the CS which goes into the datacube is different

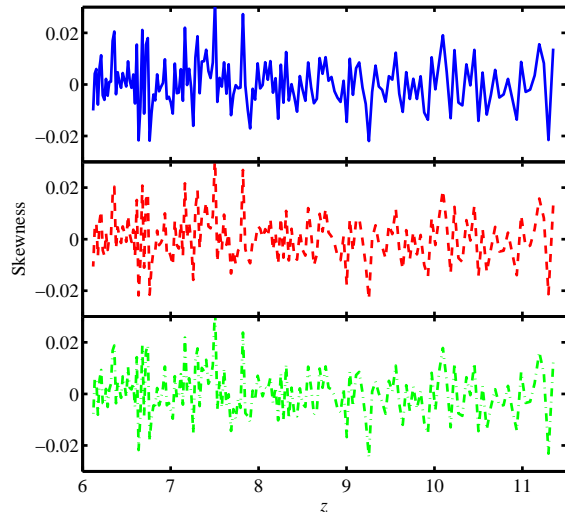


Figure 4. Skewness of the fitting residuals from datacubes with uncorrelated noise. The same noise is used in each cube. The colours and styles of the lines are the same as in Fig. 2: in the top panel, the component of the datacube from the CS comes from f250C; in the middle panel, from the T-QSO simulation; and in the bottom panel, from the T-star simulation. The similarity between the three panels arises because the noise realization (and the foregrounds) is the same for each panel, and dominates over the CS.

for each panel of the plot, the noise and foregrounds are the same. This accounts for the fact that the skewness as a function of redshift shows very similar features in each panel. At first sight this seems rather discouraging, with the desired signal totally dominated by fitting errors (FEs) and noise.

The situation can be improved, however. At each frequency, we may denoise the residual image by smoothing. This is possible because our images are oversampled, with more than one pixel per resolution element, and because there are no pixel-to-pixel correlations in the noise (by construction). While this is clearly unrealistic, it serves as a prototype for the more difficult denoising step when we consider the dirty maps. The effect of smoothing on the different components of the residual maps – these components being the CS, FEs and noise – is illustrated in Fig. 5, in which we show how the absolute value of the third moment of the one-point distribution of these components, $|\mu_3|$, is affected when they are smoothed with windows of different size. We show the result for the slice of the T-star datacube at 115 MHz, corresponding to a redshift of 11.35. This slice is chosen because the skewness of the T-star simulation is significantly negative here; we get similar results with the other simulations if we choose an appropriate slice in which the skewness is significantly different from zero. When the smoothing window is very narrow, so that there is almost no smoothing, $|\mu_3|$ for the noise exceeds the value for the CS. This occurs even though $\langle \mu_3^{\text{noise}} \rangle = 0$ (where the expectation is taken over different noise realizations), simply because the noise *rms* is so much larger than that of the (significantly skewed) cosmological signal. As the size of the smoothing window is increased, $|\mu_3^{\text{noise}}|$ drops much more quickly than $|\mu_3^{\text{CS}}|$ since the smoothing averages together uncorrelated noise pixels, but correlated signal pixels. At large scales, the signal also becomes uncorrelated, so its small *rms* means that $|\mu_3^{\text{CS}}| < |\mu_3^{\text{noise}}|$ once more. The scale at which $|\mu_3^{\text{CS}}|$ exceeds $|\mu_3^{\text{noise}}|$ by the greatest amount in this residual map is approximately 3–4 arcmin. In the case of the fitting errors, $|\mu_3^{\text{FE}}|$

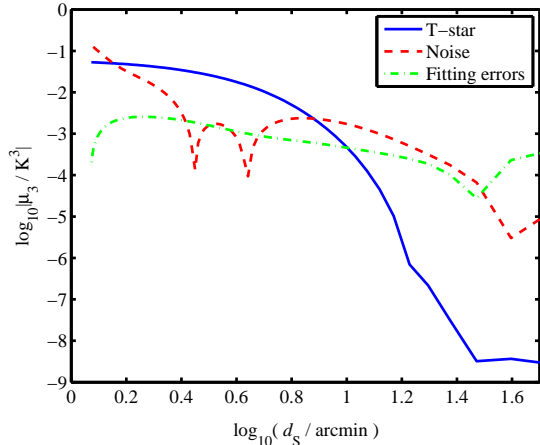


Figure 5. The effect of smoothing scale on the absolute value of the third moment of the one-point distribution, $|\mu_3|$ (defined in Equation 1), for the three different components of the residual maps at 115 MHz ($z = 11.35$). The width, d_S , of the Gaussian distribution which forms our smoothing kernel is defined here as the distance between $x = \pm\sigma$ for a distribution with standard deviation σ . The CS (blue, solid line) is from the T-star simulation, in which the skewness of the one-point distribution is negative at this frequency. The red, dashed line corresponds to the noise (where here the noise on each pixel in the unsmoothed map is independent), and the green, dot-dashed line to the fitting errors, by which we mean the difference between the foregrounds cube and the polynomial fit to the full datacube. The value for the foregrounds themselves, before fitting, is several orders of magnitude larger.

shows less variation as the smoothing scale is changed than either of the other components. If the foreground fitting were completely unbiased, we might expect that any errors in the fitting would be Gaussian and caused entirely by noise, and so this component of the residual images would behave similarly to the noise component. The fact that the skewness in the fitting errors appears to come partly from large scales suggests that bias in the fitting may allow some leakage through from the foregrounds themselves, which are correlated on large scales. If the skewness of the foregrounds is larger than we have assumed, therefore, we will need to fit them more accurately in addition to exploiting this scale dependence. In the present case, $|\mu_3^{\text{FE}}|$ is similar to $|\mu_3^{\text{noise}}|$ at the scale at which the latter is dwarfed by the contribution from the CS.

In practice, to extract the skewness as a function of frequency we make the natural choice of smoothing scale, using the same kernel as was used to degrade the signal and foregrounds to the resolution of the telescope. We then compute the skewness in each slice as before. The skewness as a function of frequency for each datacube, after following this procedure, is shown in Fig. 6. To improve the clarity of the plot, each line is smoothed by taking a moving average with a span of nine points (a boxcar filter). To estimate the error, we generate 100 datacubes containing the foregrounds and with different realizations of the noise, but with no CS present. We feed each cube through our fitting and smoothing procedure, calculate the skewness as a function of redshift, and smooth this function with a moving average filter just as for the cubes containing a signal. The range between the 16th and 84th percentile of the skewness for these realizations is shown as the light grey shaded area in the figure.

One can see from Fig. 6 that this smoothing procedure allows us to extract a significant signal, despite making only rather general

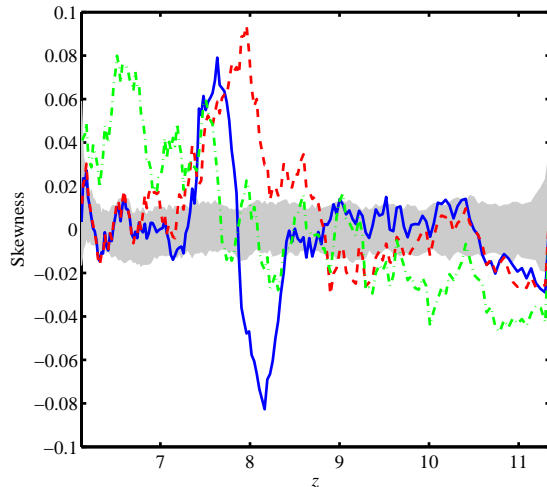


Figure 6. Skewness of the fitting residuals from datacubes with uncorrelated noise, but in which the residual image has been denoised by smoothing at each frequency before calculating the skewness. The three lines correspond to the three simulations, with colours and line styles as indicated in Fig. 2. Each line has been smoothed with a moving average (boxcar) filter with a span of nine points. The grey, shaded area shows the errors, estimated using 100 realizations of the noise. The fact that the lines differ so much is in marked contrast to Fig. 4, and shows the impact of smoothing the residual images to suppress the noise.

assumptions about the scale at which features due to the signal, instrument and noise are important. The result for f250C (blue, solid line) is most striking, with rapid transitions in the skewness in the range $z \approx 7.5$ – 8.5 . The position of the dip corresponds to the position of the dip in the uncorrupted simulation shown in Fig. 2. While the skewness continues to rise in the original simulation, however, for the extracted signal it returns to zero at low redshift. This is because the variance of the CS becomes very small at low redshift. In the uncorrupted simulation, this allows the skewness to grow very large. In the residual images, however, the variance of the noise and fitting residuals comes to dominate, even after smoothing, which drives the skewness towards zero. We return to this point below when we consider alternative statistics. The extracted signal for the other two simulations shows the behaviour one might expect: the T-QSO simulation (red, dashed line) shows only a weak dip in skewness, but a strong peak due to the rapid rise in skewness for the uncorrupted simulation at $z \lesssim 8.5$. The T-star simulation, meanwhile, shows a gradual rise in skewness throughout the redshift range, with significant non-zero skewness detected for $z \gtrsim 9.5$ and $z \lesssim 7.5$.

4.3 Skewness from dirty maps

We now move on to an analysis of the so-called ‘dirty maps’. To generate these, we first add together the unsmoothed foreground and signal cubes, where the latter have been tiled, as before, to produce maps of the right angular size. Each slice is then corrupted by the instrumental response. We achieve this in practice by Fourier transforming the image, multiplying by the sampling function (calculated on a grid with the same number of points as the image), and then applying the inverse Fourier transform. This is equivalent to convolving each image with the point spread function (PSF) of

the instrument. We make the simplifying assumption that the sampling function does not change with frequency. If the uv plane is uniformly filled, this should not be excessively optimistic. It could be enforced in practice by discarding high- k data so that equivalent (and completely filled) areas of the uv plane are retained in each frequency band. The noise is dealt with slightly differently. We consider pixels in the uv plane where the sampling function is non-zero to be encompassed by our uv coverage, and we generate uncorrelated Gaussian noise at each such pixel. Pixels outside our uv coverage are set to zero. We (inverse) Fourier transform to return to the image plane, then normalize this ‘noise image’ such that it has the correct *rms*. This procedure yields noise that is almost uncorrelated between independent resolution elements (though the noise on adjacent pixels is correlated).

We fit out the foregrounds in the dirty cubes in the same way as before. The skewness of the residual images exhibits the same problem seen in Fig. 4, being dominated by the noise. In this case, the smoothing procedure used above would not be expected to help, since the noise is correlated on the scale of our smoothing kernel. In addition, since our resolution is comparable to the scale of features in the original signal, using a broader kernel simply washes out the signal as well as the noise. We therefore require a more sophisticated denoising scheme.

4.3.1 Wiener filtering

With the results of Section 4.2 in mind, we use the differing correlation properties of the signal and noise in our extraction. To be explicit, suppose that we write the residuals as a vector \mathbf{d} , where d_i is the residual at the i th pixel of a map at a given frequency. We relate \mathbf{d} to the image from the uncorrupted simulation, \mathbf{s} , by

$$\mathbf{d} = \mathbf{R}\mathbf{s} + \boldsymbol{\epsilon} \quad (4)$$

The matrix \mathbf{R} encodes the convolution of the signal with the PSF, while $\boldsymbol{\epsilon}$ represents the noise. We neglect any contribution to $\boldsymbol{\epsilon}$ coming from errors in the fitting procedure, so we can assume that the correlation matrix of the noise, $\mathbf{N} = \langle \boldsymbol{\epsilon}\boldsymbol{\epsilon}^\dagger \rangle$, is known (here, $\boldsymbol{\epsilon}^\dagger$ is the conjugate transpose of $\boldsymbol{\epsilon}$).

We consider a very optimistic situation for extracting the skewness, which occurs if the correlation matrix of the signal, $\mathbf{S} = \langle \mathbf{s}\mathbf{s}^\dagger \rangle$, is also known. We can then perform a Wiener deconvolution on each residual image to recover an estimate of the CS. That is, we compute $\hat{\mathbf{s}} = \mathbf{F}\mathbf{d}$ where the Wiener filter \mathbf{F} is given by

$$\mathbf{F} = \mathbf{S}\mathbf{R}^\dagger(\mathbf{R}\mathbf{S}\mathbf{R}^\dagger + \mathbf{N})^{-1} \quad (5)$$

(see, e.g., Zaroubi et al. 1995). In the absence of noise, this procedure reduces to an ideal inverse filter that estimates the original image before corruption by the PSF. In the presence of noise, the Wiener filter suppresses power in the image at those values of k for which the signal-to-noise ratio (SNR) is low, while retaining power for modes where the SNR is high (see, e.g., Press et al. 1986). The algorithm is optimal in the least-squares sense.

The skewness of these deconvolved images as a function of redshift is shown in Fig. 7. Comparing to Figs. 2 and 3, one can see that this procedure gives excellent results, recovering the general trends in skewness seen in the original simulations. Indeed, using an optimal filter with precise knowledge of the signal and noise properties means that we recover larger values for the skewness than were seen after applying the simple smoothing to the uncorrelated noise case of Section 4.2 (Fig. 6). We can realistically expect a situation intermediate between the results of Figs. 4 and 7. The lines representing f250C and the T-QSO simulation do not extend

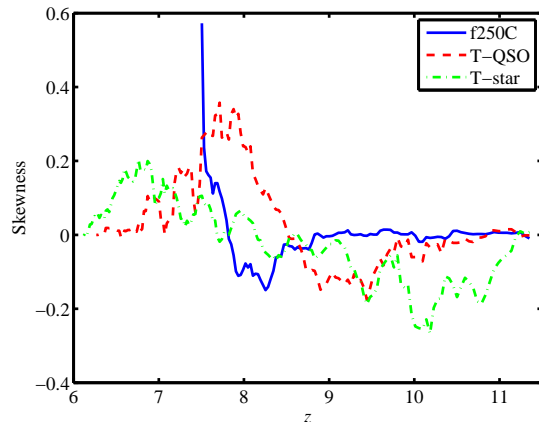


Figure 7. Skewness of deconvolved images as a function of redshift. The dirty maps are generated by convolving the CS and foregrounds with the instrumental response, and adding noise with a realistic correlation matrix. The CS is then estimated by fitting out the foregrounds and applying a Wiener deconvolution to the residuals, assuming that the PSF and the correlation matrices of signal and noise are known. Line colours and styles are the same as in Fig. 2. The deconvolution (as opposed to the simple smoothing which was sufficient for the uncorrelated noise used in Fig. 6) is unstable when the cosmological signal becomes very small, which prevents us from estimating the errors in the same way as for Fig. 6.

all the way to $z = 6$ in Fig. 7. At these redshifts, the variance in the CS is so small compared to that of the noise that the deconvolution becomes unstable. For the same reason, we cannot estimate the errors in the same way as for Fig. 6 (that is, by generating realizations with no CS at all). None the less, the errors can be inferred to be small since we do not see the same effect as in Fig. 6, in which the extracted signal from the datacube generated with the f250C and T-QSO simulations is very similar at high and low redshift, being dominated by noise.

An obvious objection to the method presented here is that if the correlation matrix of the CS is known, this means that we have already detected a signal from the EoR, so higher-order statistics are not required to extract it. The force of this objection depends on how good an estimate of the correlation matrix of the signal is required for the deconvolution to give an acceptable result. We present a test of this in Fig. 8. The three lines in the figure show the skewness extracted from the f250C residuals using three different assumptions for the correlation matrix, \mathbf{S} , used in the Wiener deconvolution. The solid, blue line shows, for reference, the skewness extracted when we use the correct correlation matrix $\mathbf{S}_{\text{f250C}}(z)$, calculated from the original simulation, in performing the deconvolution. The dashed, magenta line shows the extracted skewness when we use $\frac{1}{2}\mathbf{S}_{\text{f250C}}(z)$ instead. Underestimating the correlation matrix by a factor of two clearly has only a minimal effect on the extraction of the skewness. Finally the dot-dashed, cyan line shows the result when we use the correlation matrix of the T-star simulation. Even though the redshift evolution of the two simulations is very different, the dip and peak in the skewness at $z \approx 7.5$ – 8.5 are recovered, though it is not clear that they can be easily distinguished from the spurious variations at high redshift. This preliminary result is encouraging, but it would be preferable to use a correlation matrix estimated from the data themselves. For example, writing Equation 5 in terms of the correlation matrix of the residuals, $\mathbf{D} = \langle \mathbf{d}\mathbf{d}^\dagger \rangle$, it becomes

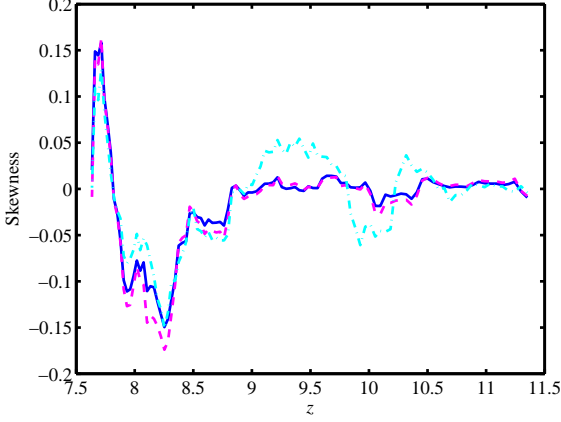


Figure 8. The skewness as a function of redshift recovered from the f250C simulation by Wiener deconvolution, using three different assumptions for the correlation matrix, \mathbf{S} , of the original signal. For the solid, blue line we use the correct correlation matrix, $\mathbf{S}_{f250C}(z)$. For the dashed, magenta line we use $\frac{1}{2}\mathbf{S}_{f250C}(z)$, and for the dot-dashed, cyan line we use the correlation matrix from the T-star simulation.

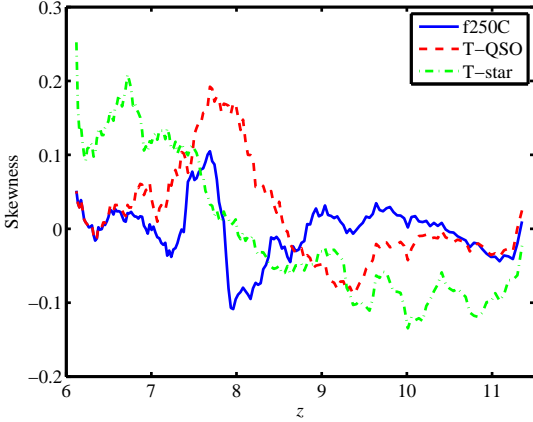


Figure 9. Skewness of dirty maps with realistic noise, but in which no foregrounds have been added. This is equivalent to a case in which we achieve perfect removal of the foregrounds.

$$\mathbf{F} = \mathbf{R}^{-1}(\mathbf{D} - \mathbf{N})\mathbf{D}^{-1} \quad (6)$$

Unfortunately this filter does not work so well in practice, since the convolution means that important small-scale information present in \mathbf{S} is not present in \mathbf{D} . Since estimation of the signal correlation matrix is intimately connected with techniques for power spectrum estimation, we defer further investigation to a future paper.

4.3.2 Foreground subtraction effects

Part of the need for sophisticated denoising techniques comes from the fact that imperfect fitting of the foregrounds introduces errors into our residual images. We illustrate this in Fig. 9, in which we show the skewness of the dirty maps to which we have added realistic noise, but no foregrounds. The main trends in the evolution of the skewness are clearly visible. We have seen in Fig. 4 that even uncorrelated noise prevents us from recovering a signal if we first

have to subtract the foregrounds. Therefore it is the combination of bright foregrounds and structured noise which prevents us from extracting the skewness without some assumptions about the properties of the signal. It will therefore be important to develop further our techniques for foreground subtraction, and to test how sensitive they are to variations in our models for the foregrounds.

4.4 Skewness from Fourier space data

The observable quantity for an interferometer is the radio visibility: a quantity that lives in Fourier space. It also seems natural, therefore, to try to extract a signal from the EoR without transforming to the image plane first (though we note that some stages of the analysis which must be completed to produce the clean datacube from which we attempt to extract a signal, such as the subtraction of bright point sources, are also carried out in the image plane). For example, Datta et al. (2007) have presented a formalism to search for bubbles in 21cm data using a statistic on the visibilities.

Unfortunately, it is not convenient to calculate the skewness from Fourier space data. The case for the moments of the density field is well known: the variance of the overdensity field, $\langle \delta^2 \rangle$, is equal to the two-point correlation function evaluated at zero separation, $\xi(0)$, which in turn is equal to an integral over the power spectrum of fluctuations. Similarly, the third moment $\langle \delta^3 \rangle$ is equal to $\zeta(0, 0)$ where $\zeta(\mathbf{r}_1, \mathbf{r}_2) \equiv \langle \delta(\mathbf{x})\delta(\mathbf{x} + \mathbf{r}_1)\delta(\mathbf{x} + \mathbf{r}_2) \rangle$. Then we have

$$\zeta(0, 0) = \int d^3\mathbf{k}' d^3\mathbf{k}'' B(\mathbf{k}', \mathbf{k}'', -\mathbf{k}' - \mathbf{k}'') \quad (7)$$

where B is the bispectrum, defined by

$$\langle \tilde{\delta}(\mathbf{k}_1)\tilde{\delta}(\mathbf{k}_2)\tilde{\delta}(\mathbf{k}_3) \rangle \equiv \delta_{\mathbf{D}}(\mathbf{k}_1 + \mathbf{k}_2 + \mathbf{k}_3)B(\mathbf{k}_1, \mathbf{k}_2, \mathbf{k}_3) \quad (8)$$

where $\tilde{\delta}(\mathbf{k})$ is the Fourier counterpart of $\delta(\mathbf{x})$ and $\delta_{\mathbf{D}}$ is the Dirac delta-function. The bispectrum is a rather unwieldy object to grapple with in this context. Foreground extraction is also problematic: while the foregrounds remain smooth as a function of frequency at a given uv point, the angular scale sampled by that point is also a function of frequency. Further consideration of Fourier space statistics is therefore beyond the scope of this paper.

4.5 Alternative statistics

The potential for using the skewness of the CS to help in the extraction invites the question of whether other one-point statistics, such as the kurtosis, could also be useful. We define the kurtosis here as $\mu_4/\sigma^4 - 3$ where μ_4 is the fourth central moment of the distribution, and we subtract 3 so that a Gaussian distribution has a kurtosis of zero. In fact the kurtosis does evolve strongly in the signal simulations. As was the case for the skewness, it is not difficult to see why. While the brightness temperature traces the density field it retains a kurtosis similar to that of a Gaussian distribution. The formation of bubbles then produces a bimodal distribution with no strong central peak, so the kurtosis, a measure of the ‘peakiness’ of the distribution, is reduced. In the final stages of reionization, the distribution becomes strongly peaked around zero, with a tail of points with strong emission, leading to a large kurtosis. The evolution of the kurtosis is therefore qualitatively similar to that of the skewness. We see all these stages in our simulations, and the evolution of kurtosis as a function of redshift is shown in Fig. 10. Unfortunately these trends seem to be much harder to recover than in the case of skewness. While we can weakly recover the dip for the case of uncorrelated noise in the image plane, using a similar procedure to

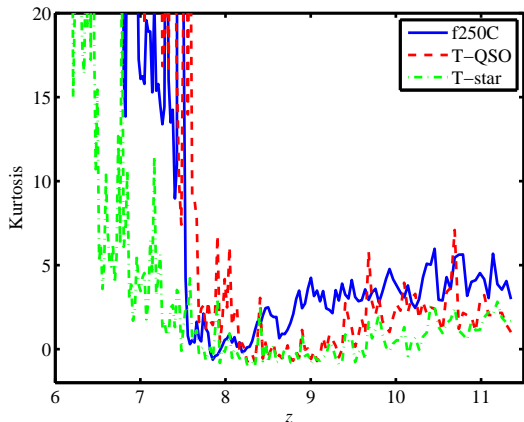


Figure 10. The evolution of the kurtosis of the distribution of δT_b as a function of redshift in our three simulations. Some of the qualitative features are similar to those seen in the skewness in Fig. 2, though for slightly different reasons which are explained in the main text. In the definition of kurtosis used here, a Gaussian distribution has a kurtosis of zero. As in the lower panel of Fig. 3 we cut off the very large values at low redshift, in order to make the high redshift region clearer.

that used for Fig. 6, we cannot recover the low-redshift peak. For the dirty maps, the dip in kurtosis cannot be seen even after the optimistic deconvolution used in Fig. 7.

Because most of the variance in the unsmoothed residual images comes from the noise and fitting errors, which one might expect not to be skewed, we have investigated whether or not the unnormalized third moment, μ_3 , might perform better than the skewness, μ_3/σ^3 , for signal extraction. In fact we find that they perform similarly, but the results for the skewness tend to be easier to interpret. This is because to calculate the errors we must still estimate the expected spread in μ_3 from the random noise, and hence have an estimate of the *rms* of the noise. Because the noise power changes with frequency, the errors also become frequency dependent: the shaded area in a figure analogous to Fig. 6 no longer has constant width.

5 DISCUSSION

We have demonstrated that the skewness could be a useful tool for signal extraction in the presence of realistic overall levels of foregrounds and noise. It could be, though, that some aspect we have not accounted for makes the process more difficult. For example, while the foreground maps we use have *rms* fluctuations of the correct magnitude, they have rather low levels of skewness, perhaps unrealistically low. If, instead, the foregrounds turn out to be very skewed, then unless the algorithm to fit out foregrounds is unbiased, this could propagate into the fitting residuals and drown out the CS. In this case, however, the characteristic pattern in the skewness as a function of redshift – a dip followed by a peak – may allow the signal to be picked out even in the presence of residuals from the foregrounds. This would be exploiting the smoothness of the foregrounds as a function of frequency once more.

As pointed out by Jelić et al. (2008), data constraining the characteristics of the foregrounds at the relevant scales and frequencies are quite scarce (though see, for example, Pen et al. 2008). None the less, the extrapolations we make from larger scales and

higher frequencies may be pessimistic, if anything. Moreover, the structured noise appears to be at least as influential as the foreground fitting residuals in limiting the sensitivity of our signal extraction using the skewness. For other statistics, great care may be required to model and remove the foregrounds to high accuracy (Morales, Bowman & Hewitt 2006). Dealing with polarized foregrounds is also a concern, which will be approached in future work.

Clearly, it is also desirable to model the CS itself accurately, especially when using higher order statistics. A good extraction scheme should work for a wide range of reionization scenarios, and ideally should be able to distinguish between them. We have therefore tested our scheme with three detailed models in which the ionization history is quite different. Though in each case we see the skewness become relatively small before rising to large values – behaviour which may be generic – a more extended period of reionization stretches out these features. It is possible, however, that more exotic sources which we have neglected would cause different behaviour. If, for example, decaying dark matter makes a significant contribution to heating the intergalactic medium before reionization or during its early stages, we can expect this heating to be uneven, the rate of energy deposition depending on the square of the density. Then we can no longer assume that the hydrogen spin temperature, T_s , is much larger than the CMB temperature, T_{CMB} , everywhere. We would have to multiply Equation 3 by a position-dependent factor $(T_s - T_{\text{CMB}})/T_s$, which could result in non-zero skewness even if the neutral fraction is approximately unity everywhere.

The main limitation of these simulations when it comes to testing our extraction scheme, however, is their size. To generate maps with the area of one LOFAR EoR window we must tile our datacubes in the image plane. In some cases this may be unrealistic: when the size of individual ionized bubbles becomes comparable to the size of the simulation box, a slice through the box can no longer be considered to be a representative slice of the Universe. We have argued that this may not be important for one-point statistics (and if anything, having a larger number of independent volumes contributing to each image would improve our signal to noise ratio). Firstly, each pixel is in any case affected differently by foregrounds and noise which are much larger than the CS. Secondly, nearby frequency slices are at a similar stage of reionization but may otherwise be sufficiently weakly correlated that smoothing along the frequency direction after extraction can help recover a clearer trend. Spatial statistics will clearly be more seriously affected by tiling. Note that there are also periodic repetitions in the frequency (redshift) direction in the simulated CS. This can be seen in the high redshift portion of the curve corresponding to the evolution of $\langle \delta T_b \rangle$ in the f250C simulation in Fig. 3. The onset of reionization appears to break this periodicity somewhat: for example, the mean ionized fraction can change significantly between two redshifts separated by a comoving radial distance corresponding to the size of the simulation box. It therefore seems to be no obstacle to robustly recovering the overall trends.

6 SUMMARY AND CONCLUSIONS

Many statistics have been put forward to characterize the 21cm emission from the EoR, the power spectrum probably being the most frequently studied (Barkana 2008; Lidz et al. 2008; Pritchard & Loeb 2008; Sethi & Haiman 2008, to choose some recent examples). We have suggested that higher-order statistics may be useful not only to characterize a CS cube that has been cleaned

of foregrounds, noise and instrumental effects, but also to extract the signature of reionization from these corrupting influences in the first place. The skewness of the one-point distribution of brightness temperature, measured as a function of observed frequency (or equivalently as a function of redshift), is one such promising statistic.

The three detailed simulations of reionization which we have studied show a strong evolution of the skewness with redshift. Some of the features of this evolution appear to be generic and can be readily understood: in the early stages of reionization the skewness drops below that of the underlying density field as the first ionized bubbles, from which the emission is negligible, are formed. As reionization progresses, the majority of the volume becomes ionized and the skewness increases again, becoming very large at low redshift when the distribution of brightness temperature is peaked at zero, with a tail extending to large values. In simulation f250C there is a well defined dip in the skewness with a width $\Delta z \approx 1$. Our other simulation in which the Universe is reionized entirely by stars (T-star) shows a more gradual change, with the epoch of reionization extending throughout the redshift range probed by LOFAR. A third simulation, T-QSO, in which QSOs reionize the Universe, shows an intermediate behaviour.

By combining these simulations with models of the foregrounds, noise and instrumental response, we have generated datacubes which are intended to simulate the output of the LOFAR EoR experiment. We have studied two cases: firstly, one in which we smooth the foregrounds and signal to the resolution of the telescope using a Gaussian kernel, then add uncorrelated Gaussian noise; secondly, one in which we degrade the foregrounds and noise to the resolution of the telescope using a realistic PSF, and add noise which is uncorrelated in the Fourier plane rather than the image plane, producing what we refer to as ‘dirty’ images. In the former case, we can see the signature of reionization in the skewness by fitting out the foregrounds to obtain residual images, and then denoising these images with a simple smoothing operation. The skewness in these images as a function of redshift shows significant evidence of reionization. The result is quite robust to the details of the foreground fitting and the smoothing. Under- or over-fitting the foregrounds affects the recovered skewness less severely than the recovered variance. Extracting a signal from the dirty cubes requires a more sophisticated denoising scheme. In an optimistic scenario where the correlation matrices of the original signal and of the noise are known, we can again recover the evolution of the skewness quite cleanly using Wiener deconvolution.

We have touched upon some areas for improvement: simulations which remain realistic but extend to larger scales and exhibit an even greater range of reionization histories; taking into account the polarization of the foregrounds and the instrumental response, and incorporating new observational constraints as they arrive; testing the minimal assumptions we must make about the signal in order for our extraction scheme to work, for example whether a poor estimate of the correlation matrix of the CS seriously affects the extracted skewness; and studying a wider range of statistics beyond the variance and power spectrum. All of these will be areas for future work. Even at this stage, however, our results justify some optimism that the new generation of radio telescopes can detect the signature of reionization using higher-order statistics.

ACKNOWLEDGMENTS

GH is supported by a grant from the Netherlands Organisation for Scientific Research (NWO). As LOFAR members, the authors are partially funded by the European Union, European Regional Development Fund, and by ‘Samenwerkingsverband Noord-Nederland’, EZ/KOMPAS. GM and II acknowledge that this study was supported in part by Swiss National Science Foundation grant 200021-116696/1 and Swedish Research Council grant 60336701.

REFERENCES

- Barkana R., 2008, MNRAS, submitted (arXiv:0806.2333)
 Barkana R., Loeb A., 2001, Physics Reports, 349, 125
 Benson A. J., Sugiyama N., Nusser A., Lacey C. G., 2006, MNRAS, 369, 1055
 Bharadwaj S., Ali S. S., 2005, MNRAS, 356, 1519
 Bromm V., Larson R. B., 2004, ARA&A, 42, 79
 Ciardi B., Ferrara A., White S. D. M., 2003, MNRAS, 344, L7
 Ciardi B., Madau P., 2003, ApJ, 596, 1
 Ciardi B., Stoehr F., White S. D. M., 2003, MNRAS, 343, 1101
 Datta K. K., Bharadwaj S., Choudhury T. R., 2007, MNRAS, 382, 809
 Di Matteo T., Perna R., Abel T., Rees M. J., 2002, ApJ, 564, 576
 Dunkley J. et al., 2008, ApJS, accepted (arXiv:0803.0586)
 Evrard A. E. et al., 2002, ApJ, 573, 7
 Fan X., Carilli C. L., Keating B., 2006, ARA&A, 44, 415
 Field G. B., 1958, Proc. Inst. Radio Eng., 46, 240
 Field G. B., 1959, ApJ, 129, 536
 Furlanetto S. R., Oh S. P., Briggs F. H., 2006, Physics Reports, 433, 181
 Furlanetto S. R., Zaldarriaga M., Hernquist L., 2004a, ApJ, 613, 16
 Furlanetto S. R., Zaldarriaga M., Hernquist L., 2004b, ApJ, 613, 1
 Gleser L., Nusser A., Benson A. J., 2008, MNRAS, 391, 383
 Gleser L., Nusser A., Ciardi B., Desjacques V., 2006, MNRAS, 370, 1329
 Hogan C. J., Rees M. J., 1979, MNRAS, 188, 791
 Iliev I. T., Mellema G., Pen U.-L., Bond J. R., Shapiro P. R., 2008, MNRAS, 384, 863
 Iliev I. T., Mellema G., Pen U.-L., Merz H., Shapiro P. R., Alvarez M. A., 2006, MNRAS, 369, 1625
 Jelić V. et al., 2008, MNRAS, 389, 1319
 Jenkins A., Frenk C. S., White S. D. M., Colberg J. M., Cole S., Evrard A. E., Couchman H. M. P., Yoshida N., 2001, MNRAS, 321, 372
 Kaiser N., 1987, MNRAS, 227, 1
 Kumar A., Subramanian K., Padmanabhan T., 1995, JA&AS, 16, 83
 Labropoulos P. et al., 2009, MNRAS, submitted (arXiv:0901.3359)
 Lidz A., Zahn O., McQuinn M., Zaldarriaga M., Hernquist L., 2008, ApJ, 680, 962
 Loeb A., Barkana R., 2001, ARA&A, 39, 19
 Madau P., Meiksin A., Rees M. J., 1997, ApJ, 475, 429
 Mellema G., Iliev I. T., Alvarez M. A., Shapiro P. R., 2006a, New Astronomy
 Mellema G., Iliev I. T., Pen U.-L., Shapiro P. R., 2006b, MNRAS
 Merz H., Pen U.-L., Trac H., 2005, New Astronomy, 10, 393
 Morales M. F., Bowman J. D., Hewitt J. N., 2006, ApJ, 648, 767

- Morales M. F., Hewitt J., 2004, *ApJ*, 615, 7
- Oh S. P., Mack K. J., 2003, *MNRAS*, 346, 871
- Peebles P. J. E., 1980, *The large-scale structure of the universe*. Princeton Univ. Press, Princeton, NJ
- Pen U.-L., Chang T.-C., Peterson J. B., Roy J., Gupta Y., Hirata C. M., Odegova J., Sigurdson K., 2008, *MNRAS*, submitted (arXiv:0807.1056)
- Press W. H., Flannery B. P., Teukolsky S. A., 1986, *Numerical recipes. The art of scientific computing*. Cambridge: University Press, 1986
- Pritchard J. R., Loeb A., 2008, *Phys. Rev. D*, 78, 103511
- Scott D., Rees M. J., 1990, *MNRAS*, 247, 510
- Sethi S., Haiman Z., 2008, *ApJ*, 673, 1
- Shaver P. A., Windhorst R. A., Madau P., de Bruyn A. G., 1999, *A&A*, 345, 380
- Spergel D. N. et al., 2007, *ApJS*, 170, 377
- Springel V., 2005, *MNRAS*, 364, 1105
- Springel V., Yoshida N., White S. D. M., 2001, *New Astronomy*, 6, 79
- Thomas R. M., Zaroubi S., 2008, *MNRAS*, 384, 1080
- Thomas R. M. et al., 2009, *MNRAS*, 393, 32
- Valdés M., Ferrara A., Mapelli M., Ripamonti E., 2007, *MNRAS*, 377, 245
- Zaldarriaga M., Furlanetto S. R., Hernquist L., 2004, *ApJ*, 608, 622
- Zaroubi S., Hoffman Y., Fisher K. B., Lahav O., 1995, *ApJ*, 449, 446
- Zaroubi S., Thomas R. M., Sugiyama N., Silk J., 2007, *MNRAS*, 375, 1269